Perovskite design principles for efficient microwave dry reforming with noble metal free catalysts

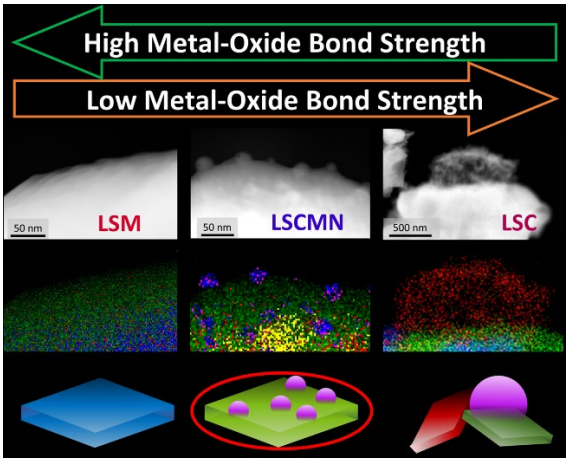

Chris M. Marin[1,2]; Eric J. Popczun[1]; Christina N. Wildfire[1]; Orhan Kizikaya[3]; Douglas R. Kauffman[1]

[1]National Energy Technology Laboratory, 626 Cochran Mill Road, Pittsburgh, PA 15236, USA

[2]NETL Support Contractor, 626 Cochran Mill Road, Pittsburgh, PA 15236, USA

[3]Center for Advanced Microstructures and Devices (CAMD), Louisiana State University, Baton Rouge, LA, 70806, USA

Keywords methane, CO_2, reforming, perovskite, microwave, exsolution, tolerance-factors

Highlights (up to 5 bullets, 85 character limit including spaces)

- Microwave absorbing perovskites are screened in the LSC-LSN-LSM ternary system
- Best performing catalysts have reducible active sites and irreducible framework
- Stability peaks at compositions that result in nearly ideal cubic perovskites
- Combined Goldschmidt and octahedral factors effective predictors of ideal catalysts
- Best performance and stability from exsolution of Ni-Co alloy active sites

Abstract

Microwave absorbing catalysts have the potential to electrify high-temperature thermal reactions such as the dry reforming of methane process (DRM: $CO_2 + CH_4 \rightarrow 2CO + 2H_2$). However, microwave catalysts

present unique challenges due to their dual requirements of maintaining microwave absorption in both oxidative and reductive environments and stability across a range of temperatures in inherently non-isothermal reactors. Here, catalyst candidates from the $La_{0.8}Sr_{0.2}CoO_3$-$La_{0.8}Sr_{0.2}NiO_3$-$La_{0.8}Sr_{0.2}MnO_3$ perovskite systems were screened (28 total) to identify promising microwave catalysts free of noble metals for dry reforming methane. The best performing candidates met two main criteria. First, they occurred at crystal phase boundaries, giving rise to a pseudocubic perovskite structure. The combined use of Goldschmidt tolerance factor and octahedral tolerance factors appeared to be suitable for predicting pseudocubic perovskites. Second, they provided a balance of reducible metal sites with an irreducible metal oxide support. The best performing catalyst was found to exsolve Ni-Co alloy particles as active sites for the DRM reaction which offered superior resistance to coking for excellent reforming efficiency and stability.

1. Introduction

Synthesis gas (syngas, CO+H_2) is so named because of its use as a precursor feedstock throughout the chemical industry, from specialty plastics and olefins to fertilizers, steel, and fuels.[1] Industrially, steam methane reforming (SMR, $CH_4 + H_2O \rightarrow 3H_2 + CO$) is the primary method of generating syngas (3:1 H_2:CO), and is responsible for 6% of all global natural gas consumption [2] with 33% of that natural gas solely providing reaction heat to drive this endothermic reaction (a full 2% of all natural gas consumed globally). [3] For chemical reactions needing a lower than 3:1 syngas ratio produced by SMR (such as for methanol or Fischer-Tropsch synthesis), the excess hydrogen is generally separated off from the product stream as waste. There are, however, additional methane reforming processes such as dry reforming methane (DRM, $CH_4 + CO_2 \rightarrow 2H_2 + 2CO$) that could be used to provide syngas at a 1:1 ratio, but DRM requires higher reaction temperatures compared to SMR making it much less cost effective due to higher energy requirements.

Microwaves provide a pathway to directly convert disparate sources of electricity into the high catalyst temperatures required for methane reforming. Electricity can come from a variety of sources (coal, solar, wind, nuclear, etc.) and microwave reactors are agnostic to the electricity source. Additionally, microwaves are a direct and selective method of heating. Since chemistry occurs on the surface of heterogeneous catalysts, heating should ideally be selectively applied to heating just the catalyst surface rather than an entire reactor volume. A high susceptibility microwave absorbing catalyst support is one

pathway for directly heating catalysts (distributed electrified heating), which can result in greatly decreased energy demands for high-temperature endothermic reactions due to energy being selectively applied to where the chemistry is taking place rather than the reactor side walls. [4] [3] Here, we report the development of a microwave susceptor/catalyst for the efficient conversion of methane to syngas by a microwave dry reforming (MW-DRM) process. The catalyst composition was based on the perovskite oxide $La_{0.8}Sr_{0.2}CoO_3$ (LSC), well known as a conductive oxide in the high temperature fuel cell field. With a melting point of ~1700 °C and conductivity comparable to graphite (4,400 S/cm [5]), LSC is an excellent microwave susceptor (material that converts microwaves to heat), but has stability issues that prevent usage in reductive conditions [6] such as microwave dry reforming [7]. However, as a perovskite, the crystal structure of LSC is able to accommodate a wide array of dopant elements which affords it a large breadth of tunability.

Ionic radii are important to the rational design of stable perovskite structures since it is known that the perovskite structure is only stable with specific ratios of ionic radii which allows for a cubic structure to occur [8] [9]. Perovskites take an overall formula of ABO_3, where A is often an alkaline earth metal or lanthanide metal, while B is often a first-row transition metal. The framework of a perovskite structure is formed by B-site metal-oxygen-metal octahedrally coordinated bonds with the A-site cation helping to charge balance the structure. Perovskites are prototypically a cubic structure, assuming equal bond lengths between transition metals and the nearest oxygen atoms. Frequently, the ideal cubic structure is distorted due to uneven bond lengths from Jahn-Teller distortion or from geometric packing constraints. Additionally, the structure prototypically has a total cation charge of +6 to counterbalance 3 O^{2-} anions, but the overall structure can tolerate a cation charge slightly below +6 by generating oxygen defects. In the case of $La_{0.8}Sr_{0.2}CoO_3$, the addition of Sr^{2+} induces oxygen defects and promotes both oxygen ion conductivity and electronic conductivity. For this work, a constant A site ratio of $La_{0.8}Sr_{0.2}$ was utilized, which results in a constant A site charge of +2.8 and an A site ionic radius of 1.376 Å. [10] By adjusting the B site dopant ratios of Ni, Co, and Mn in the catalysts for this study, the B site oxidation state could be modified from a preferred +2 (Ni) to +4 (Mn). Additionally, the average ionic radii could be modified between 0.53 Å (Mn^{4+}) and 0.69 Å (Ni^{2+}) by changing the dopant ratios. However, accurate predictors for the formation of single-phase perovskites remains an area of active research, made more critical by the discovery of new perovskite applications such as in high efficiency photovoltaics. [11] [12] [13]

Traditionally, the preferred metric for predicting the formation of a perovskite is the Goldschmidt tolerance factor (t), defined as:

$$t = \frac{r_A + r_O}{\sqrt{2}(r_B + r_O)} \qquad \text{Eq. 1}$$

where r_A, r_B, and r_O are the ionic radii of the A site, B site, and oxygen, respectively. [8] The Goldschmidt tolerance factor predicts an ideal cubic perovskite as t approaches 1.0. Since the ionic radii of the A site and of oxygen were kept fixed in this study, t was effectively adjusted between 0.94 ($La_{0.8}Sr_{0.2}NiO_3$) and 1.02 ($La_{0.8}Sr_{0.2}MnO_3$). In addition to the traditional Goldschmidt tolerance factor, other geometrically related tolerance factors have been proposed. One such addition proposed is the Octahedral factor [14] [15] [16], defined as

$$\mu = \frac{R_B}{R_O} \qquad \text{Eq. 2}$$

with the expectation that only specific ratios of R_b/R_O can geometrically support a tight (rattle free) perovskite structure.

In addition to the traditional geometric approaches to predicting the formation of perovskites, there has been a recent push to leverage machine learning methods to predict the formation of perovskites. For instance, Bartel et al. utilized an experimental dataset of 576 materials for training a model for the prediction of perovskite formation, with the machine learning derived tolerance factor (tau) being used to predict potential new material candidates when tau was less than 4.18. [17] Alternatively, Park et al. utilized machine learning to evaluate octahedral deformation parameters between doped and ideal perovskites in order to predict stability. [18] However, limited sample pools remain the norm in material science with the hope that each new small sample dataset will ultimately help guide the development of machine learning approaches for perovskite structure prediction. [19]

For microwave dry reforming (MW-DRM) catalysis, it is essential that the catalyst simultaneously provides active sites for the reaction and provides efficient microwave absorption. For promoting CO_2 adsorption, basic oxides (such as La and Sr oxides)[20, 21] are generally utilized. For adsorption and activation of methane, typically metallic particles are needed [20, 22-26]. $La_{0.8}Sr_{0.2}CoO_3$ has known instability issues in reducing conditions (such as CH_4+CO_2 or CH_4+H_2O) and will go through a series of known phase transitions [6, 7, 27, 28]. ABO_3 perovskites first phase separates into periclase (BO) and Ruddlesden-Popper (A_2BO_4, a type of layered perovskite structure), then metal (B) and Ruddlesden-Popper phases, and ultimately all the perovskitic structure is lost when the Ruddlesden-Popper phases

are reduced to metal and separate oxides (resulting in $2B+A_2O_3$). By limiting the extent of phase separation, there is an opportunity to reversibly exsolve metallic nanoparticles during reaction conditions, which provide the necessary active sites for CH_4 adsorption/disassociation and is a known method of generating anchored metal nanoparticles for catalysis [29-31]. Therefore, it is necessary to control the strength of the perovskite metal-oxygen backbone through B-site metal doping to generate a catalyst that reduces enough to reach the desired phase (identified via in-situ XRD to be $B+A_2BO_4$) [7] under the selected reaction conditions without over-reducing. For this study, the catalyst was optimized by changing the ratio of B site metal dopants between Co, Mn (for a stronger metal-oxygen bond), and Ni (for a weaker metal-oxygen bond).

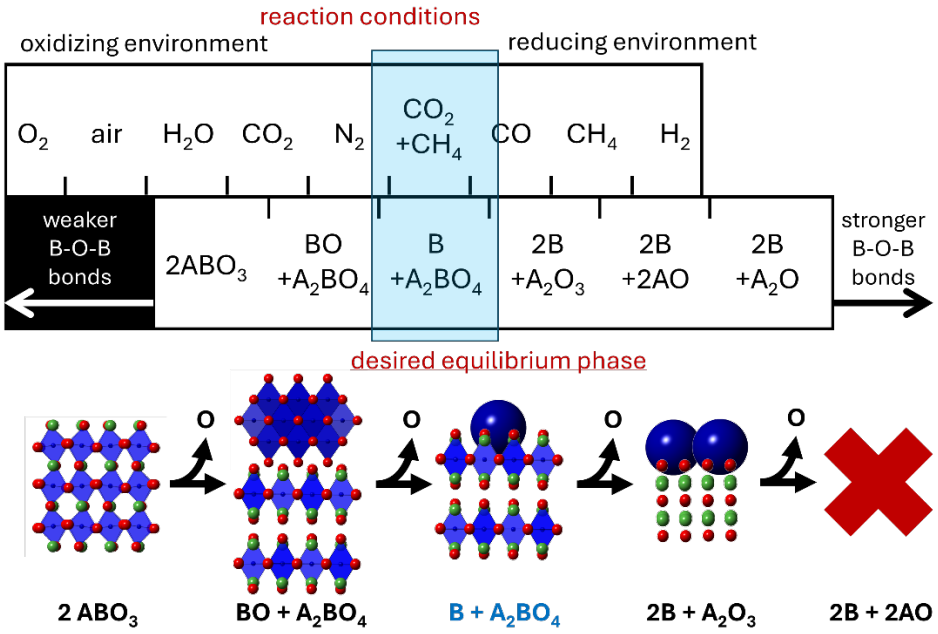

Scheme 1. Catalyst development scheme shown symbolically as a slide rule. Depending on reduction conditions, perovskite may be fully oxidized (ABO_3), or may reduce stepwise (shown with single O removals) into periclase on Ruddlesden-Popper phase ($BO + A_2BO_4$) and into metal on Ruddlesden-Popper phase ($B + A_2BO_4$). Over-reduction will result in complete separation of A and B phases as the perovskitic oxide structure is lost. In the case of a DRM catalyst, the goal is for the catalyst to equilibrate as a $B + A_2BO_4$ phase when heated under CO_2+CH_4 reaction conditions (where the blue cursor is highlighting), and reform initial ABO_3 when heated in air for complete recyclability.

Of the 28 compositions synthesized and screened for this study, the highest performing compositions were able to consume 100 kg_{CO2}/MWh and 33.2 kg_{CH4}/MWh, while demonstrating H_2 production at 110 kWh/kg_{H2} and simultaneous CO production at 8.5 kWh/kg_{CO} from dry reforming using

1 g of catalyst. The relatively large experimental pool of perovskite candidates was synthesized and tested under the same conditions. Characterization was collected by XRD and oxygen k-edge X-ray absorption spectroscopy (XAS) to check structure against tolerance factor perovskite formability predictions. Use of a Ni-Co alloy active site was found to reduce coke buildup that would otherwise impact catalyst performance, allowing for over 9 hours of operation in optimized catalysts with the small benchtop reactor. The optimized microwave catalyst was found to be completely regenerable by re-calcining under air to return metal active sites back into the parent perovskite structure with no drop in performance observed after coke removal.

2. Methods

2.1. Catalyst preparation and characterization

Since DRM requires temperatures above 900 °C to stay free of coke formation at 1 bar of pressure [32], we opted to prepare our catalysts using high-temperature solid state synthesis at a higher temperature (1100 °C) and in air. We adopted a fixed perovskite A site composition of 80% La and 20% Sr to reduce complexity and focus on the more substantial structural changes from B site composition. All catalysts screened in this study were prepared by mixing stoichiometric amounts of strontium (II) carbonate [$SrCO_3$, 99.9%, Sigma-Aldrich], lanthanum (III) oxide [La_2O_3, 99.5%, Alfa-Aesar], cobalt (II,III) oxide [Co_3O_4, 99%, Sigma-Aldrich], nickel (II) oxide [NiO, 98% Sigma-Aldrich], and/or manganese (III) oxide [Mn_2O_3, 99% Alfa-Aesar]. Mixtures were mixed and ground in an agate mortar for 10 minutes, added to a 13 mm pellet die assembly, and pressed into pellets by applying a pressure of 5 metric tons for 5 minutes using a Carver, Inc. pellet press (#4350.L). Pellets were removed from the die assembly and heated in an alumina crucible to 1100 °C at a rate of 1.5 °C/min and held for 64 hours in air at ambient pressure. Upon completion, the sample was cooled to room temperature and ground into a fine black powder with a mortar and pestle. Powder diffraction patterns for the synthesized samples were collected on a PANalytical X'Pert Pro diffractometer to confirm the starting phase. Depending on catalyst B site composition, some catalysts were not necessarily phase pure (details to follow). Scanning electron microscopy (SEM) was collected using an FEI Quanta 600F SEM and energy-dispersive X-ray spectroscopy (EDX) was collected using an Oxford Inca X-act detector. High-angle annular dark-field scanning transmission electron microscopy (HAADF-STEM and STEM-EDX) was collected using an FEI Titan Themis

G2 200. STEM samples were prepared by sonicating dilute solutions of catalyst samples in methanol and drop casting them onto holey carbon coated copper TEM grids.

2.2. X-ray absorption characterization

Soft X-ray absorption oxygen K-edge spectra of all perovskite samples were collected at the varied-line-space plane grating monochromator beamline of the Center for Advanced Microstructures and Devices (CAMD) synchrotron facility (Louisiana State University). The samples were spread onto a carbon tape placed on a stainless-steel sample holder and loaded into the main chamber via a load-lock chamber. The main chamber pressure was maintained at ~10^{-9} Torr. All absorption spectra were acquired in total electron yield mode by measuring the drain current of the sample. The O K-edge spectra were normalized and analyzed using Athena software.

2.3 Microwave dry reforming catalytic benchmarking

To rapidly optimize catalyst formulations for the microwave dry reforming of methane (MW-DRM) reaction, our approach was to test each catalyst to the point of failure using a small benchtop microwave reactor (CEM Discover SP), mass spectrometer (Pfeiffer Omnistar), and a mixture of pure CO_2 and CH_4 able to be delivered at rates up to 1,000 sccm using a reactor setup as shown in Figure 1.

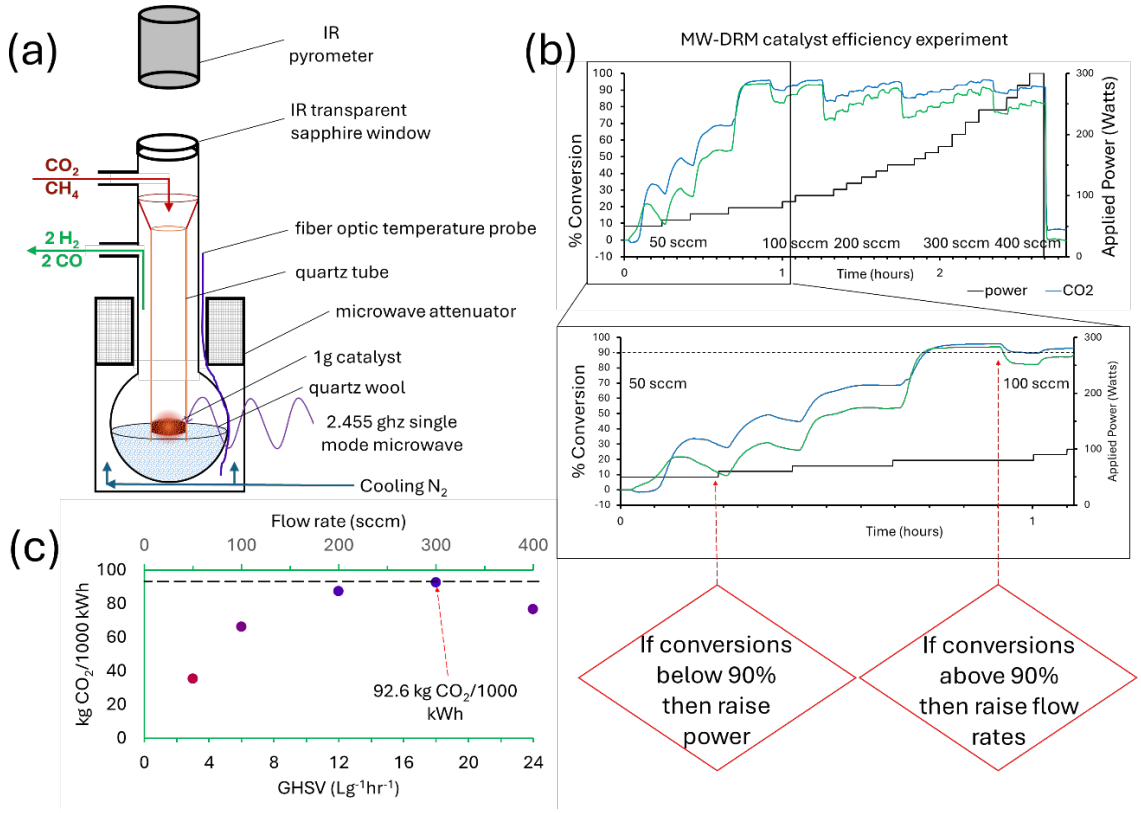

Figure 1. (a) Basic reactor schematic used in this study. All tests in this study were 1 g with the space velocity varied by changing flow rate. (b) Typical reactor test plan consisting of the applied power increased stepwise until conversions of both CO_2 and CH_4 held over 80%. Once conversions of both CO_2 and CH_4 were over 90% then the space velocity was increased. (c) Outcome of each test plan was the amount of CO_2 (and CH_4) converted per unit power at a range of space velocities for each catalyst.

In a typical test plan, gas flow was flowed through a 1 g quartz wool supported catalyst bed at 50 sccm with 50 W microwave power applied. Since side reactions such as the reverse water gas shift ($CO_2 + H_2 \rightarrow CO + H_2O$) and the Boudouard reaction ($2CO \rightarrow CO_2 + C$) are favored at temperatures below 700 °C, corresponding to equilibrium conversions below 80% of CO_2 and CH_4 [20, 32], we focused solely on conditions that allowed above 80% conversions of both CO_2 and CH_4 for evaluating dry reforming performance for each composition. If catalyst conversions were below 90% conversion for both CO_2 and CH_4, applied power was increased in a 10-20 W interval. If conversions of CH_4 and CO_2 did stabilize above 90% conversions, the reactant flow rates (and space velocity) were increased and the power was gradually stepped up to reach 90% conversions again. Effectively then, we tested for conditions in which CO_2 and CH_4 conversions were stable between 80% and 90% while increasing the space velocity in steps. This process was repeated until the system maximum of 300 W microwave power was applied with the highest performing catalysts reaching this at space velocities of 24 L/g*hr while the worst performing failed to achieve 90% conversions at just 3 L/g*hr. Finally, for each flow rate, power level, and measured percent

conversion, the dry reforming efficiency was calculated in terms of kg $CO_{2\ converted}$/MWhr where both CH_4 and CO_2 conversions were over 80% for each sample.

3. Results

3.1. LSC-LSM series

Initial tests were conducted using $La_{0.8}Sr_{0.2}CoO_3$ (LSC) with varied amount of Mn substitution on the B site from 0-100% (i.e., $La_{0.8}Sr_{0.2}MnO_3$) as shown in Table 1.

Table 1. LSCM series of catalysts.

#	Name	A site % La	A site % Sr	B site % Co	B site % Mn
1	LSC	80	20	100	0
2	LSCM 90:10	80	20	90	10
3	LSCM 75:25	80	20	75	25
4	LSCM 66:34	80	20	66	34
5	LSCM 50:50	80	20	50	50
6	LSCM 25:75	80	20	25	75
7	LSM	80	20	0	100

Pure LSC has considerable difficulty maintaining a perovskitic structure under the strongly reductive conditions of methane dry reforming. However, past studies have shown Mn helped to stabilize LSC under reductive conditions. [7] In this study, the limits of this performance gain were studied by increasing the space velocity and microwave power to find the performance limits of each catalyst (see Figure 1). In the case of LSC, peak dry reforming efficiency was reached with 80% conversions at 200 sccm (12 $Lg^{-1}hr^{-1}$) and 260W for 40.3 $kgCO_2$/MWh. The addition of 34% Mn loading to form $La_{0.8}Sr_{0.2}Co_{0.66}Mn_{0.34}O_3$ (written as LSCM 66:34) was found to improve performance to reach 80% conversions at 300 sccm (18 $Lg^{-1}hr^{-1}$) and ~190W power for 87±8 $kgCO_2$/MWh. Additional Mn loading past 34% was found to decrease the material performance with very low catalytic activity again by $La_{0.8}Sr_{0.2}MnO_3$.

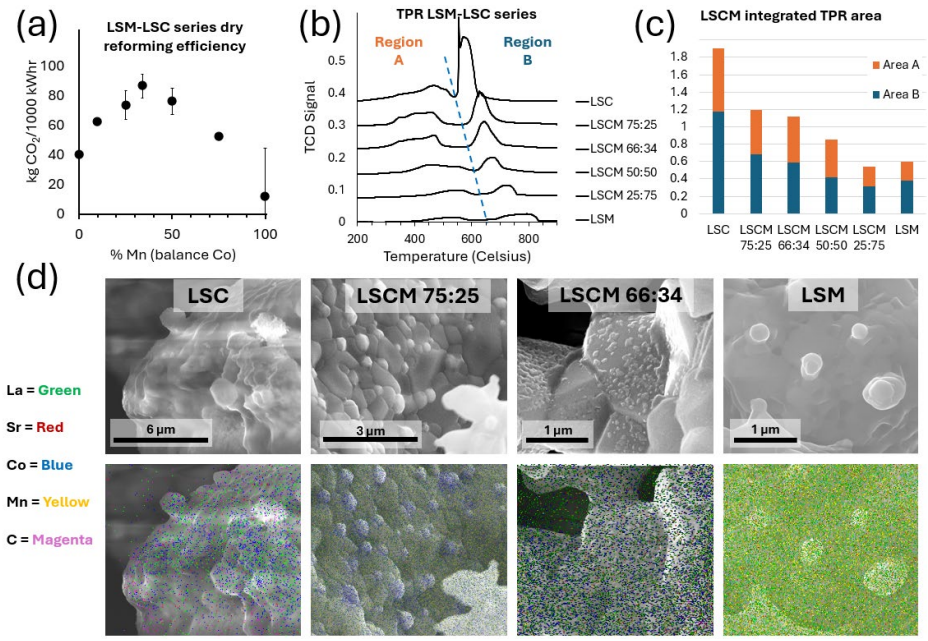

Figure 2 (a) Peak MW-DRM efficiency (test plans conducted as shown in Figure 1) for 7 compositions of perovskites ranging from $La_{0.8}Sr_{0.2}CoO_3$ to $La_{0.8}Sr_{0.2}MnO_3$. Error bars show standard deviation for compositions synthesized and tested at least 3 separate times. (b) Temperature programmed reduction experiments for perovskites ranging from LSC to LSM. Dotted line drawn to visually divide the broad low temperature reduction features (Region A) from the high temperature reduction features (Region B). (c) Integrated values of the same TPR data with the total area of region A shown in orange and the total area of region B shown in blue. (d) SEM and EDX maps of perovskite samples after testing MW-DRM efficiency ranging from LSC to LSM. Note, although surface features were visible on LSCM 66:34, the features were too small and thin for clear identification in EDX mapping, and no clear separation was visible by EDX in LSM.

In order to investigate the impact that Mn substitution has on perovskite catalyst behavior under reductive conditions, temperature programmed reduction (TPR) was collected using 10% hydrogen to reduce the catalyst. As can be seen in Figure 2b, the reduction of LSC occurs in two distinct regions. The first region has been shown to be consistent with the reduction of the ABO_3 perovskite to Ruddlesden-Popper (layered perovskite, $A_{n+1}B_nO_{3n+1}$) structures. [7] Depending on the perovskite, this can be a straightforward one step reduction as shown in scheme 1, or it may occur through a series of layered perovskite structures which leads to Region A becoming broader. For instance, $LaCoO_3$ is known to transition through $La_4Co_3O_{10}$ (an n=3 Ruddlesden-Popper) before reducing to La_2CoO_4 (n=1) [27], which would result in multiple reduction features in Region A. For LSC, the large sharp reduction feature of Region B was found to be consistent with both the formation of the desired phase of $B+A_2BO_4$ and further reduction to $2B+A_2O_3$. [7] Expectedly, substitutions of increasing amounts of Mn for Co results in

both a shift of this reduction feature for higher temperatures (Figure 2b), but also a decrease in the total reducibility of the catalyst (Figure 2c) with a notable decrease in total reducibility with Mn loading above ~34-50%. Consequently, although the addition of Mn has the desired effect of increased perovskite stability in a high temperature reducing environment, it also has the undesired effect of decreasing the amount of Co active sites that can form which are needed for a good dry reforming catalyst. [7] This can be readily visualized by SEM-EDX of the catalysts after testing for dry reforming efficiency. Post reaction, LSC was found to significantly phase separate into separate regions of Co, La, and Sr with heavy carbon buildup in the Co rich areas (Figure 2d). In contrast, a 25% Mn load on the catalyst B site resulted in clearly defined sub-micron scale Co particles on a La and Sr rich support consistent with the desired equilibrium phase of a microwave absorbing dry reforming catalyst. Further increasing the Mn content to 34% resulted in a larger number of smaller Co particles forming across the catalyst surface such that EDX mapping no longer had sufficient spatial resolution to show distinct Co regions and appeared that Co, La, Sr, and Mn remained well dispersed post reaction despite the clear surface structures visible in the SEM of LSCM 66:34. In contrast, these particles were not visible across the surface of LSM post microwave dry reforming.

3.2. LSN-LSM series

Since nickel is typically regarded as a better performing methane reforming catalyst than cobalt (and is more commonly used), [33] we investigated if the performance of $La_{0.8}Sr_{0.2}NiO_3$ (LSN) is similarly improved through the incorporation of Mn (from 0-100% as shown in Table 2).

Table 2. LSMN series of catalysts.

#	Name	A site % La	A site % Sr	B site % Mn	B site % Ni
1	LSM	80	20	100	0
2	LSMN 80:20	80	20	80	20
3	LSMN 66:34	80	20	66	34
4	LSMN 50:50	80	20	50	50
5	LSMN 20:80	80	20	20	80
6	LSN	80	20	0	100

As synthesized, LSN had poor performance for microwave dry reforming in our tests as it barely achieved 80% conversions at our lowest flowrate of 50 sccm (3 $Lg^{-1}hr^{-1}$) and at 240W (Figure 3a). Similar

to the LSC-LSM case, the addition of increasing amounts of Mn improved catalyst performance up until, in this case, 66% Mn (LSMN 66:34). The optimized LSMN was capable of >80% conversions at 200 sccm (12 $Lg^{-1}hr^{-1}$) at 100 W power for 99±8 $kgCO_2$/MWh, a significant 15% improvement in dry reforming efficiency versus the best LSCM catalyst.

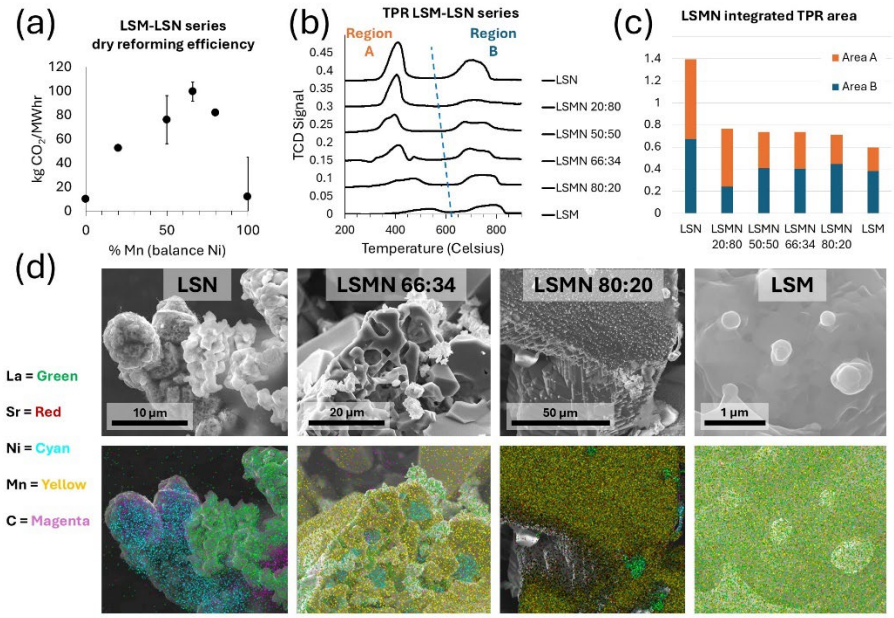

Figure 3. (a) Peak MW-DRM efficiency (test plans conducted as shown in Figure 1) for perovskites compositions ranging from $La_{0.8}Sr_{0.2}NiO_3$ to $La_{0.8}Sr_{0.2}MnO_3$. Error bars show standard deviation for compositions synthesized and tested at least 3 separate times. (b) Temperature programmed reduction experiments for perovskites ranging from LSN to LSM. Dotted line drawn to visually divide the broad low temperature reduction features (Region A) from the high temperature reduction features (Region B). (c) Integrated values of the same TPR data with the total area of region A shown in orange and the total area of region B shown in blue. (d) SEM and EDX maps of perovskite samples after testing MW-DRM efficiency ranging from LSN to LSM. LSN displayed complete phase separation of Ni from La and Sr regions with carbon coking present on Ni regions.

Performance dropped off by LSM back to 12 $kgCO_2$/MWh (250W for only 3 $Lg^{-1}hr^{-1}$). Similar to the LSC-LSM series, the addition of Mn resulted in a shift in the reduction peaks towards higher temperature with higher Mn loading although the shift was less pronounced (Figure 3b). Similarly, the total reducibility decreased with Mn loading but was relatively level between 20-80% Mn loading (Figure 3c). SEM-EDX showed very sharp differences in morphology following microwave dry reforming efficiency tests (Figure 3d). Post-reaction, LSN had complete phase separation of Ni from La and Sr with large carbon deposits on the Ni particles present. Effectively, LSN had fully over-reduced to Ni + La_2O_3 + SrO. Conversely, LSM had no clear phase separation visible by SEM-EDX following reaction. Between those

two limits, catalysts in the LSMN series showed large amounts of structural reconstruction under dry reforming conditions. At low Ni loadings, the Ni exsolved to the surface similar to Co, but the separation appeared more complete by SEM-EDX resulting in clear pockets of just Ni and regions of heavily reconstructed La, Sr, and Mn (unlike the LSCM system which tended to still keep Co partially mixed in the Mn regions). By 34% Ni loading, phase separation resulted in a hollowed-out mixture of materials that nonetheless retained better dispersion of nickel particles than at higher Ni loadings, but this structural reconstruction likely was responsible for the poorer catalytic performance at high space velocities compared to the LSM-LSC series even though the efficiency at 12 $Lg^{-1}hr^{-1}$ was higher.

3.3. LSCMN series with Mn:Ni fixed 2:1

Since the LSM-LSN series displayed the highest performance at a 2:1 ratio, initial catalyst screening was performed with this Mn:Ni ratio fixed with the balance of Co varied between 0 and 100% (Table 3).

Table 3. LSCMN series of catalysts with Mn:Ni ratio held at 2:1.

#	Name	A site % La	A site % Sr	B site % Co	B site % Mn	B site % Ni
1	LSC	80	20	100	0	0
2	LSCMN 92.5:5:2.5	80	20	92.5	5	2.5
3	LSCMN 85:10:5	80	20	85	10	5
4	LSCMN 70:20:10	80	20	70	20	10
5	LSCMN 55:30:15	80	20	55	30	15
6	LSCMN 40:40:20	80	20	40	40	20
7	LSCMN 25:50:25	80	20	25	50	25
8	LSCMN 10:60:30	80	20	10	60	30
9	LSMN 66:34	80	20	0	66	34

The overall highest efficiency catalyst remained the cobalt-free $La_{0.8}Sr_{0.2}Mn_{0.66}Ni_{0.34}O_3$. However, performance was comparable (within standard deviation of each other) with Co concentrations below 50% on the perovskite B site (Figure 4a).

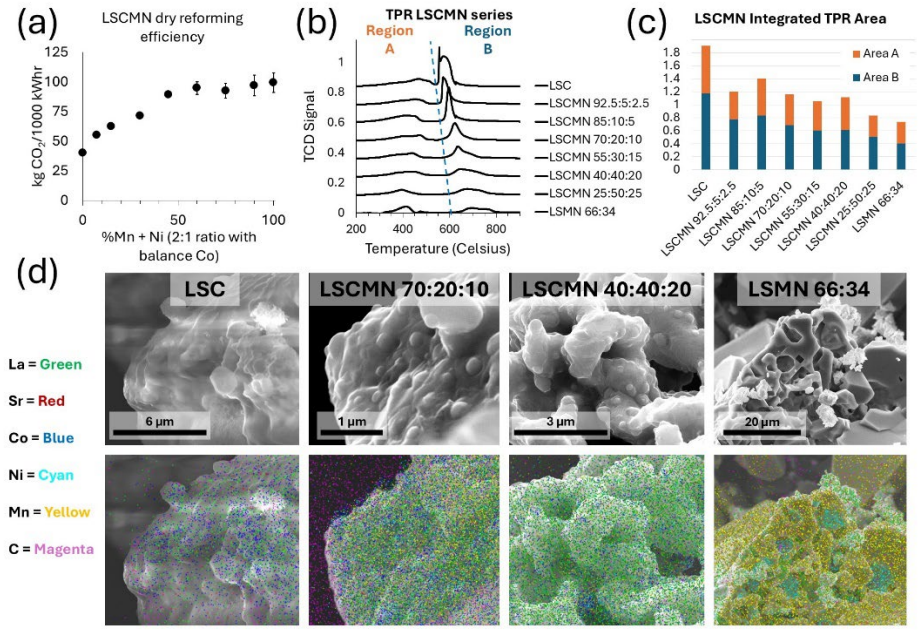

Figure 4. (a) Peak MW-DRM efficiency (test plans conducted as shown in Figure 1) for perovskites compositions ranging from $La_{0.8}Sr_{0.2}CoO_3$ to $La_{0.8}Sr_{0.2}Mn_{0.66}Ni_{0.34}O_3$. Error bars show standard deviation for compositions synthesized and tested at least three separate times. (b) TPR experiments for perovskites ranging from LSC to LSMN 66:34. Dotted line drawn to visually divide the broad low temperature reduction features (Region A) from the high temperature reduction features (Region B). (c) Integrated values of the same TPR data with the total area of region A shown in orange and the total area of region B shown in blue. (d) SEM and EDX maps of perovskite samples after testing MW-DRM efficiency ranging from LSC to LSMN 66:34. LSCMN displayed clearly socketed particles at the surface that were small enough to be difficult to clearly EDX map by SEM.

Unlike LSMN 66:34, Co doped catalysts efficiency peaked at 18 $Lg^{-1}hr^{-1}$ for 25-40% Co loadings. TPR showed a consistent shift to higher temperatures for Region B reduction with increasing Mn loading (Figure 4b). However, the total reducibility remained relatively high up until Mn content was increased above 40% (Figure 4c). Similar to the LSC-LSM series, SEM-EDX showed clear exsolved particles on the catalyst surface post MW-DRM testing (Figure 4d). For larger particles visible in $La_{0.8}Sr_{0.2}Co_{0.7}Mn_{0.2}Ni_{0.1}O_3$ (LSCMN 70:20:10, Figure 4d), it appeared that Co and Ni were co-exsolving as alloy particles. For further verification, STEM-EDX was conducted on LSCMN 40:40:20 post MW-DRM testing (Figure 5).

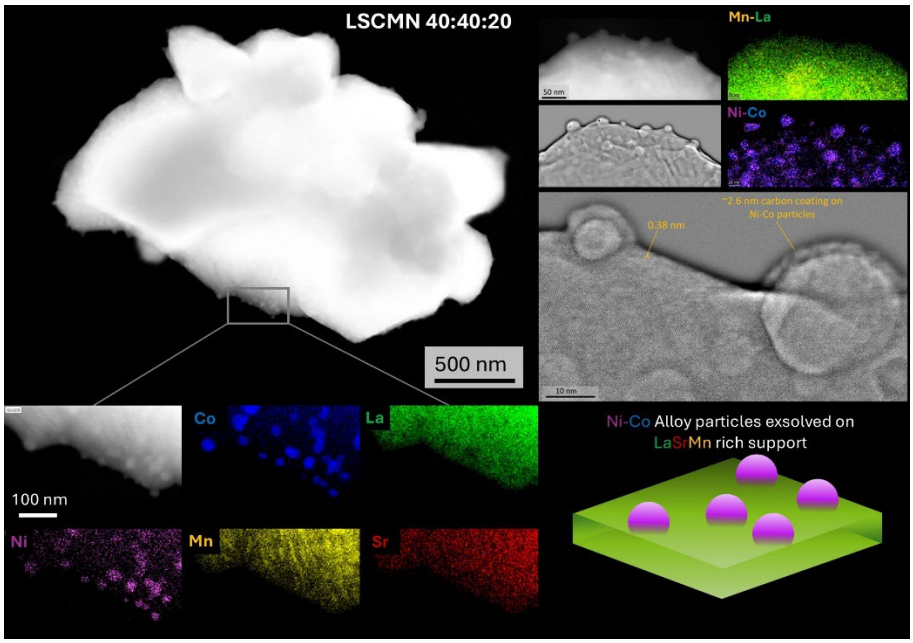

Figure 5. HAADF-STEM imaging of a typical microscale particle of $La_{0.8}Sr_{0.2}Co_{0.4}Mn_{0.4}Ni_{0.2}O_3$ after testing MW-DRM. Although the particle is bulk, reduction under reaction conditions resulted in fine nanoparticles diffused across the bulk perovskitic microparticle. Nanoparticles appeared to be entirely Ni-Co alloy particles as separate Ni or Co particles were not observed. Use of a high-pass filter for the image showed an amorphous carbon coating was clearly present on the Ni-Co nanoparticles with relatively uniform thickness while $LaMnSrO_x$ support appeared clear of this amorphous coating.

The surfaces of the microscale catalyst particles were coated with exsolved Ni-Co particles and at no location were separate Ni or Co particles observed, even with the sub-50 nm nanoparticles clearly visible through STEM-EDX. Unlike in the LSM-LSN system, the remaining perovskite support in the LSCMN system did not appear to become dramatically hollowed out and reconstructed as significant amounts of Co remained with the LSM support even post dry reforming at the microwave's maximum of 300W (consistent with what was observed with the LSM-LSC series catalysts). Essentially, the use of both Co and Ni provided the benefits of both systems with the superior activity of the Ni active sites in the LSM-LSN system along with the better support stability and better catalyst space velocities of the LSM-LSC system.

3.4. Impact of tolerance factors on structure and function

Characterization of the perovskite structures were collected by XRD and XAS. For the LSC-LSM system, both LSC and LSM index purely as perovskites (Figure 6a, Figure s1). However, the perovskites that both LSC and LSM index as are not cubic, instead adopting the rhombohedral distorted R-3c

structure. This rhombohedral structure is still a perovskite – the structure is composed of vertex sharing metal oxide octahedra making up the B-O-B bonding backbone with the A-site cations ionically bonding and filling the voids in the structure. However, Jahn-Teller distortions in the transition metals results in unequal metal-oxygen covalent bond lengths which results in irregular octahedra and manifests in XRD as split peaks. [34] This is most pronounced looking at the strongest diffraction peak (011) at ~33° (which splits into $1\bar{1}0$ and 211 for the rhombohedral structure, shown Figure 6a inset). Unlike LSC and LSM, compositions in between became closer to an ideal cubic perovskite structure. Using XAS to look specifically at the oxygen k-edge to explore the B-O-B bonding network (since in perovskites, oxygen is bonded to b-site transition metals only), an ideal cubic perovskite is expected to show just one peak in the region between 527-531 eV. [35] [36] [37] In the case of LSCM 66:34, which had the highest tolerance factor in the LSC-LSM series while having an octahedral factor >0.414, the XAS spectrum very nearly showed just one peak at ~530 eV with a very small shoulder at 529 eV. This is in contrast to LSC, which had a large peak at 528.5 eV along with at 530.5, consistent with two types of metal oxide bonds due to the Jahn-Teller effect. LSM similarly had a very broad XAS spectrum, likely also due to two separate peaks, albeit closer together in energy.

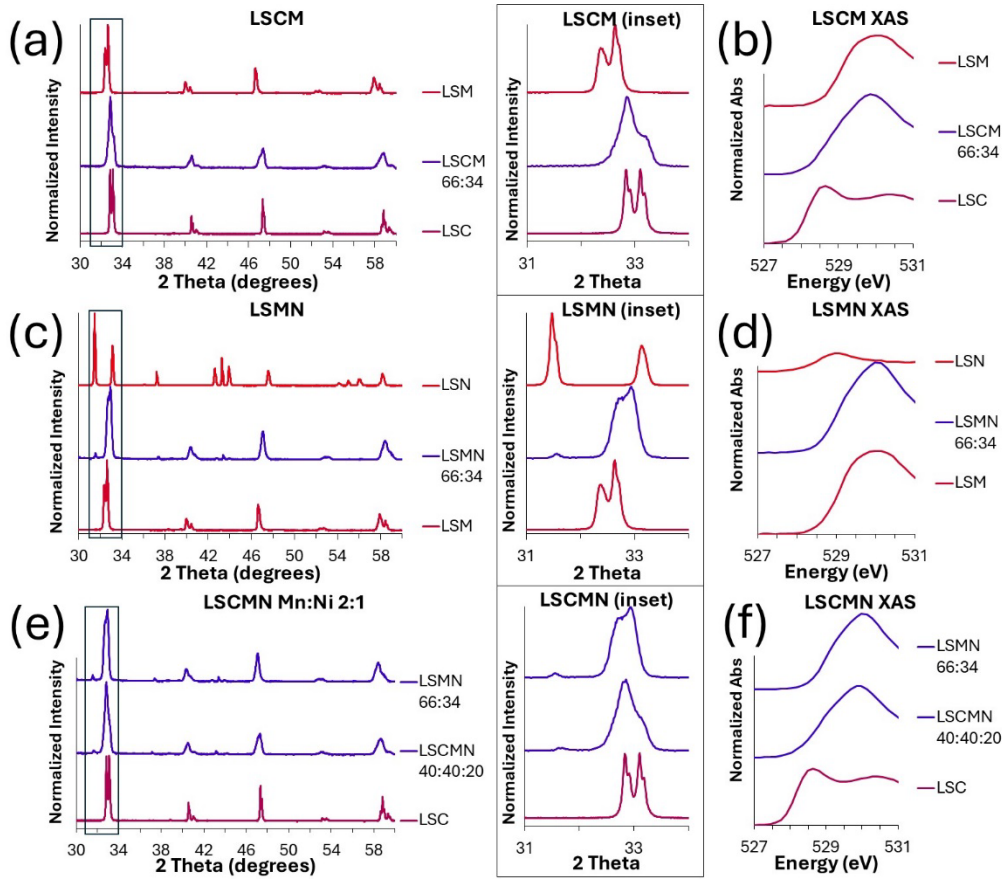

Figure 6. (a) XRD patterns for LSM, LSC, and LSCM 66:34. (inset a) Magnification of the boxed area between 31° and 34° showing the peak splitting present on the rhombohedral perovskite structures of LSC and LSM with the almost merged main peak of LSCM 66:34. (b) XAS spectrum of O k-edge between 527 and 531 eV for LSC, LSCM 66:34, and LSM. (c) XRD patterns of LSN, LSM, and LSMN 66:34 with inset showing the split main perovskite peak of LSM, the nearly cubic perovskite peak of LSMN 66:34, and the two main peaks of the Ruddlesden-Popper present in the two phase LSN system. (d) XAS spectrum of O k-edge between 527 and 531 eV for LSN, LSMN 66:34, and LSM. (e) XRD patterns for LSMN 66:34, LSCMN 40:40:20, and LSC (LSCMN series with Mn:Ni ratio 2:1). (inset e) Magnification between 31° and 34° highlighting the non-split main peak of LSMN 66:34 and LSCMN 40:40:20. (f) XAS of LSMN 66:34 and LSCMN 40:40:20 showing their non-split oxygen k-edge peaks in contrast with rhombohedral LSC.

Unlike the LSM-LSC series, the LSM-LSN series transitions from single phase perovskite (albeit rhombohedrally distorted) to a two-phase system for LSN (Figure 6c). In particular, the catalysts with Ni loadings above ~34% indexed as a mixture of $La_{2-x}Sr_xNiO_4$ and NiO (essentially meaning that synthesis conditions were insufficient to oxidize the system into pure $La_{0.8}Sr_{0.2}NiO_3$). Note that even at 34% Ni loading, a small $La_{2-x}Sr_xNiO_4$ impurity peak is visible at 31.5° which is completely gone by 20% Ni (Figure s2). $La_{0.8}Sr_{0.2}NiO_3$ would be expected to have a tolerance factor of 0.94 and an octahedral factor of 0.49. As noted, Ni had difficulty supporting the ~3+ oxidation state required for forming $La_{0.8}Sr_{0.2}NiO_3$. When the Mn concentration is increased, the tolerance factor increases to 0.99 at LSMN 66:34 before the octahedral factor drops below 0.414 as LSM is approached. This is also captured in the XAS characterization as LSN lacked the characteristic oxygen k-edge peaks in the region expected for perovskites, LSM had a broad feature consistent with multiple oxygen bond energy levels, while the highest performing LSMN 66:34 catalyst had very nearly a single peak at 530 eV (Figure 6d).

The LSCMN system similarly was found to repeat the same structural trends. With the Mn:Ni ratio fixed at 2:1, Co concentrations below 40% were found to have nearly no rhombohedral peak splitting at 33° (Figure 6e, Figure s3). Likewise, XAS showed a single peak in the 527-531 eV region for compositions in this range (Figure 6f, Figure s3). Overall, the best performing catalysts all were found to have nearly ideal tolerance factors (~0.99) while also having octahedral factors >0.414 which resulted in nearly ideal cubic perovskites without the Jahn-Teller distortion induced rhombohedral perovskite structures of LSC or LSM and without the phase separation observed near LSN.

3.5. LSC-LSM-LSN ternary system

A total of 28 samples were ultimately prepared of varied Co, Mn, and Ni loadings (as shown in Table 4) in order to fill out the compositional space of a pseudotrinary phase diagram.

Table 4. The 28 $La_{0.8}Sr_{0.2}CoMnNiO_3$ compositions prepared in this study.

#	Name	Co	Mn	Ni	R_b [1]	R_b/R_O [2]	t [3]	kgCO2/MWh[4]	Color
1	LSC	100	0	0	0.61	0.43571	0.97659	40.3	**R174 B81**
2	LSCM 90:10	90	10	0	0.602	0.43000	0.98049	62.5	**R130 B125**
3	LSCM 75:25	75	25	0	0.59	0.42143	0.98641	72.0	**R111 B144**
4	LSCM 66:34	66	34	0	0.5828	0.41629	0.98999	86.8	**R81 B174**
5	LSCM 50:50	50	50	0	0.57	0.40714	0.99642	76.3	**R102 B153**
6	LSCM 25:75	25	75	0	0.55	0.39286	1.00664	52.4	**R150 B105**
7	LSM	0	100	0	0.53	0.37857	1.01707	21.3	**R212 B43**
8	LSMN 80:20	0	80	20	0.562	0.40143	1.00048	82.0	**R91 B164**
9	LSMN 66:34	0	66	34	0.584	0.41743	0.98919	99.4	**R56 B199**
10	LSMN 50:50	0	50	50	0.61	0.43571	0.97659	75.9	**R103 B152**
11	LSMN 20:80	0	20	80	0.658	0.47000	0.95381	52.4	**R150 B105**
12	LSN	0	0	100	0.69	0.49286	0.93921	9.8	**R235 B20**
13	LSCMN 92.5:5:2.5	92.5	5	2.5	0.608	0.43429	0.97756	55.2	**R145 B110**
14	LSCMN 85:10:5	85	10	5	0.606	0.43286	0.97854	62.5	**R130 B125**
15	LSCMN 70:20:10	70	20	10	0.602	0.43000	0.98049	71.4	**R112 B143**
16	LSCMN 55:30:15	55	30	15	0.598	0.42714	0.98246	89.3	**R76 B179**
17	LSCMN 40:40:20	40	40	20	0.594	0.42429	0.98443	94.8	**R65 B190**
18	LSCMN 25:50:25	25	50	25	0.59	0.42143	0.98641	92.6	**R70 B185**
19	LSCMN 10:60:30	10	60	30	0.586	0.41857	0.98839	97.1	**R61 B194**
20	LSCMN 70:10:20	70	10	20	0.618	0.44143	0.97272	86.4	**R82 B173**
21	LSCMN 75:20:5	75	20	5	0.598	0.42714	0.98246	61.0	**R133 B122**
22	LSCMN 80:10:10	80	10	10	0.61	0.43571	0.97659	48.3	**R158 B97**
23	LSCMN 65:30:5	65	30	5	0.59	0.42143	0.98641	88.1	**R79 B176**
24	LSCMN 10:80:10	10	80	10	0.61	0.43571	0.97659	52.4	**R150 B105**
25	LSCMN 20:20:60	20	20	60	0.642	0.45857	0.96129	64.9	**R125 B130**
26	LSCMN 33:33:33	33	33	33	0.6039	0.43136	0.97956	85.5	**R84 B171**
27	LSCN 75:25	75	0	25	0.63	0.45000	0.96697	45.2	**R165 B90**
28	LSCN 50:50	50	0	50	0.65	0.46429	0.95754	3.3	**R248 B7**

[1] Average b-site ionic radius

[2] Octahedral factor

[3] Goldschmidt tolerance factor

[4] Peak MW-DRM energy efficiency achieved for each catalyst

The color assignments in Table 4 are based on the peak achieved MW-DRM performance in terms of kg_{CO2}/MWh converted while maintaining ≥ 80% conversions of both CO_2 and CH_4. For all 28 compositions, XRD was collected along with XAS of most of the compositions focused in particular on the oxygen k-edge between 528-580 eV as this region is key for understanding the transition metal-oxide bonding network of the perovskite. [35] [36] [37] [7] From XRD, all 28 samples were found to be classifiable as either rhombohedral perovskites, nearly cubic perovskites (pseudo-cubic), or were found to not form single phase perovskites and instead form a mixture of Ruddlesden-Popper and periclase phases consistent with a reduced perovskite as shown in Scheme 1 (Figure s1-s4 for XRD patterns). Additionally, the Goldschmidt tolerance factor (t) and octahedral factor (R_b/R_o) were calculated for each perovskite based on Shannon ionic radii [10] assuming an ideal 6-coordination number for the B-site metals and ionic charges of Mn^{4+}, Co^{3+}, and Ni^{2+}. Figure 6a shows all 28 tested LSC-LSM-LSN compositions from Table 4 in a ternary diagram. As shown in the LSCM, LSMN, and LSCMN series in Figures 2-4 (with these series highlighted in green on the ternary plot in Figure 6a), the perovskite catalyst activities all drop off as the composition approaches pure LSM, LSN, or LSC.

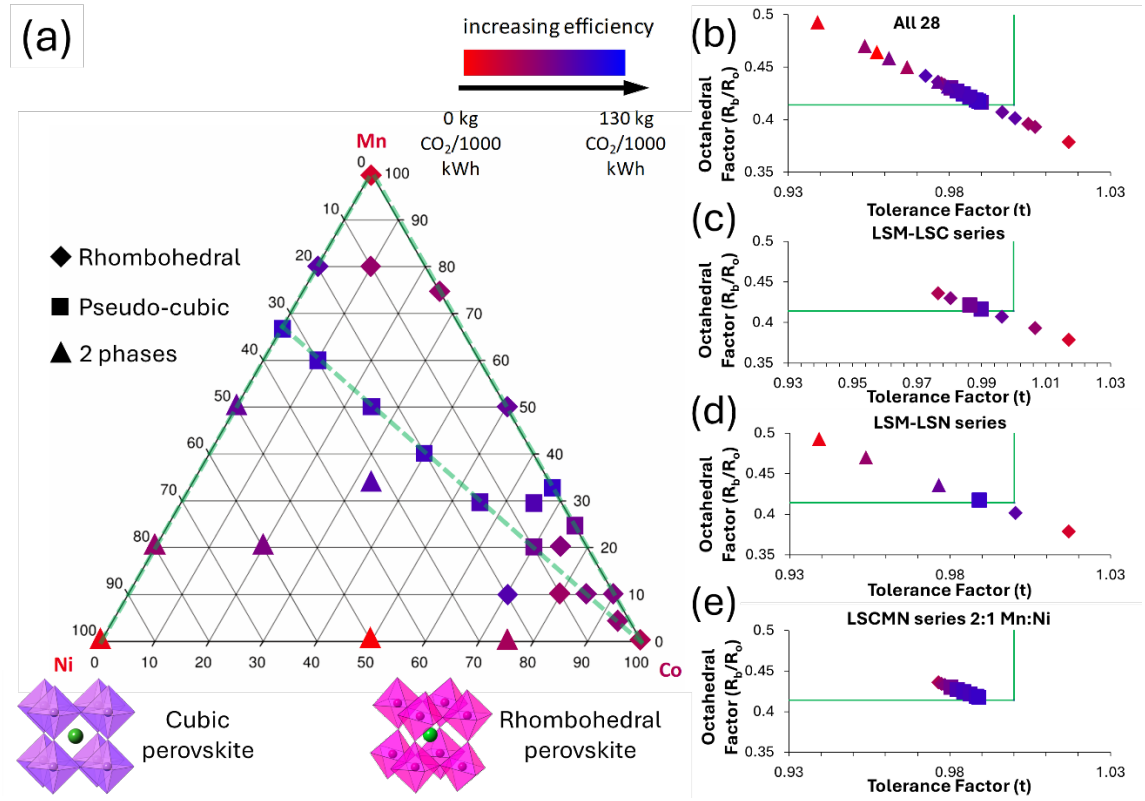

Figure 7. (a) Pseudoternary plot of all 28 perovskite compositions as a function of perovskite B site metal identity (since all compositions had the same $La_{0.8}Sr_{0.2}$ A site composition) with color assignments shown in Table 4. Marker shape shows XRD determined structure, whether rhombohedral or pseudo-cubic. Triangles show 2-phase systems where mixtures of A_2BO_4+BO formed instead of a single-phase perovskite. (b) Goldschmidt tolerance factor vs. octahedral tolerance factor plots for all 28 perovskite compositions with color assignments from Table 4. Green vertical line drawn at t=1 with horizontal line drawn at R_b/R_O= 0.414. (c-e) Goldschmidt tolerance factor vs. octahedral tolerance factor plots for the LSCM, LSMN, and LSCMN series highlighted with green lines in the pseudoternary plot.

Plotting all 28 compositions in terms of their calculated Goldschmidt tolerance factors vs. their octahedral factors, all 28 compositions make up a diagonal line (Figure 7b). This is a consequence of this study varying only the catalyst B site identity as changing the effective B site ionic radius (R_b) affects both the octahedral factor and the tolerance factor while changing the A site identity affects only the tolerance factor but not the Octahedral factor. As clearly visible in Figure 7b-e, catalyst performance improves up until roughly 0.99, gets slightly lower between 0.99-1, and performance drops off rapidly for tolerance factors above 1.0 (such as for LSM at t=1.017). The traditional Goldschmidt tolerance factor would predict that perovskites should be most stable at t=1 (shown as the vertical green limit line in Figures 7b-e). More recently it has been discussed that additional geometric constraints would require that the octahedral factor R_b/R_O must be at least $\sqrt{2}-1$ (~0.414) in order to form, [15] with this

octahedral limit shown as the horizontal limit line in Figures 7b-e. Essentially, perovskite activity is improving as the Goldschmidt tolerance factor approached 1, up until the octahedral goes below the octahedral limit of ~0.414. In terms of the LSM-LSC series (Figure 7c), the perovskite expected to be closest to ideal is LSCM 66:34 (t=0.99, μ=0.416). For the LSM-LSN series (Figure 7d), the perovskite expected to be closest to ideal then is LSMN 66:34 (t=0.99, μ=0.417), which is also the closest to ideal in the LSCMN range shown in Figure 7e. The limit lines provided by the Goldschmidt tolerance factor and octahedral factors were found to be effective predictors for catalytic performance, which corresponded well with near cubic perovskite structures. However, they were found to not be effective predictors of the formation of singe phase rhombohedral perovskite structures (for instance LSM had t=1.02 despite excellent crystallinity) and give false positives for 2-phase systems such as LSMN 50:50 which were well within the thresholds expected for a perovskite to form. However, alternative perovskite tolerance factors such as the Tau factor [17] were found to be less suitable for predicting perovskite formations as all 28 samples prepared in this study were within the range expected for single phase perovskites with Tau factors varying only modestly between 2.21 and 2.42, well less than the 4.18 limit proposed for perovskites to form within (Figure s5). For this material system at least, Goldschmidt tolerance factors and octahedral factors appeared best able to predict the ratios of Mn, Ni, and Co that could be prepared in good stable cubic perovskites.

3.6. Stability of LSCM, LSMN, and LSCMN systems

The best performing catalysts $La_{0.8}Sr_{0.2}Co_{0.66}Mn_{0.34}O_3$ (LSCM 66:34) and $La_{0.8}Sr_{0.2}Mn_{0.66}Ni_{0.34}O_3$ (LSMN 66:34) along with $La_{0.8}Sr_{0.2}Co_{0.4}Mn_{0.4}Ni_{0.2}O_3$ (LSCMN 40:40:20) were tested for stability for the microwave heated dry reforming reaction in order to test whether the reaction was best performed with Co, Ni, or Co-Ni alloy metal sites. As discussed previously, LSMN 66:34 had the highest peak efficiency reached out of the 28 catalysts in this study at 99.4 ± 8 kg_{CO2}/MWh (alternatively, 109.5 kWh/kg_{H2} generated). This was slightly higher than that observed for LSCMN 40:40:20 (94.8 ± 5 kg_{CO2}/MWh, 114.9 kWh/kg_{H2}), and significantly higher than that observed for LSCM 66:34 (86.8 ± 8 kg_{CO2}/MWh, 125.4 kWh/kg_{H2}). However, as discussed previously, this efficiency peaked for LSMN 66:34 at 12 $Lg^{-1}hr^{-1}$ while LSCM and LSCMN peaked at 18 $Lg^{-1}hr^{-1}$. For consistency, we selected a constant power and space velocity for all three catalysts at 210W applied power and 18 $Lg^{-1}hr^{-1}$ since at these conditions the conversion of CO_2 and CH_4 would start at over 80%. At these conditions, initial conversions for LSCM 66:34 were higher as shown in Figure 8a. However, CH_4 conversion rapidly

dropped off to around 80% within 5 hours. Similarly, LSMN 66:34 (Figure 8b) had conversions that rapidly dropped off within 3 hours (note again, 18 $Lg^{-1}hr^{-1}$ is a higher space velocity than LSMN most efficiently operated at). In contrast, LSCMN 40:40:20 was able to run under these conditions for twice as long as LSCM 66:34 (Figure 8c). With a separate run stopped after ~3 hours at 210W, the coke content built up on the catalysts from LSCMN 40:40:20 and LSMN 66:34 was investigated by temperature programmed oxidation (TPO) to quantify the CO_2 released from burning off the coke with the results shown in Figure 8d.

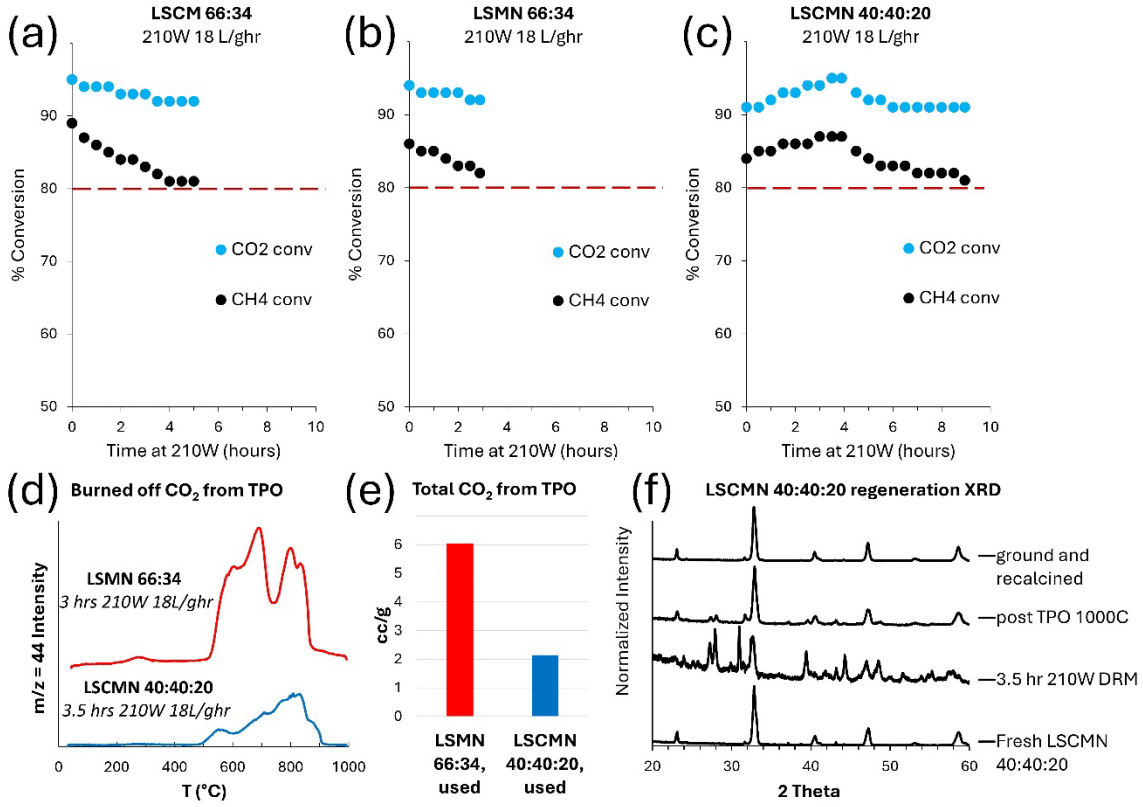

Figure 8. (a-c) MW-DRM stability tests of LSCM 66:34, LSMN 66:34, and LSCMN 40:40:20 (respectively) while operating at 210W, 1g catalyst, 18 $Lg^{-1}hr^{-1}$ (300 sccm CO_2+CH_4, ~34,000 hr^{-1}) after initially ramping up to conditions as shown in Figure 1. Note: LSCMN 40:40:20 had to be run over 2 days with the reactor off overnight. (d) TPO profiles of LSMN 66:34 after running the above stability experiment and of LSCMN 40:40:20 after repeating a stability experiment to stop after an equivalent ~3 hours. (e) Mass spectrometry quantification of CO_2 released from sample TPO back calculated for total carbon content. (f) XRD of fresh LSCMN 40:40:20, after MW-DRM, after TPO, and after reoxidation with a furnace held at 1000 °C.

In roughly the same amount of time, three times higher coke build up occurred on the Ni metal site catalyst as compared to the Ni-Co alloy metal site catalyst. Post TPO, XRD characterization showed that in addition to the carbon being burned off by 1000 °C, the LSCMN 40:40:20 catalyst's phase transitions

were almost completely reversed (Figure 8f) as Ni and Co were re-absorbed into the perovskite matrix and the Ruddlesden-Popper structure returned to a nearly pure perovskite. This could be encouraged by regrinding the catalyst and calcining for longer (12 hrs, 1000 °C), which resulted in a complete regeneration of the pseudo-cubic perovskite structure of the initial LSCMN 40:40:20. Retesting the regenerated catalyst, the LSCMN 40:40:20 performed at exactly the same efficiency as the initial testing (Figure s6) indicating that the phase transitions that took place under reaction conditions were completely reversible through regeneration by air calcination.

4. Conclusions

The LSC-LSM-LSN ternary perovskite system has been investigated and optimized for the MW-DRM reaction. In order to function as dry reforming catalysts, LSC and LSN based catalysts need to reduce and form metal particles for CH_4 activity. However, we have found that for efficient operation the amount of metal reduction must be moderated by balancing high temperature stability (resisting over-reduction and excessive phase separation) with a large amount of well anchored (sintering resistant) active sites. Due to the dual requirements of phase stability with maintaining a large number of active sites, the optimal amounts of both Co additions and of Ni additions to the largely irreducible LSM system were found to correlate with the amounts that resulted in Goldschmidt tolerance factors closest to 1 without resulting in octahedral tolerance factors dropping below $\sqrt{2}-1$. Consequently, catalytic performance was found to correlate with the formation of nearly cubic perovskite structures with minimal Jahn-Teller distortion observed in oxygen bond strengths of optimized compositions. Nickel-based catalysts were found to be more active for dry reforming than Co catalysts, but Co based catalysts supported higher space velocities. Use of both Co and Ni dopants resulted in Ni-Co alloy active sites and provided the activity of the Ni system with better stability than the Co system for efficient performance at 95 kg_{CO2}/MWh (115 kWh/kg_{H2} or 10.4 kWh/m^3_{H2}) while operating at space velocities of up to 24 $Lg^{-1}hr^{-1}$ (~45,000 hr^{-1}). At 18 $Lg^{-1}hr^{-1}$ (~34,000 hr^{-1}), $La_{0.8}Sr_{0.2}Co_{0.4}Mn_{0.4}Ni_{0.2}O_3$ was found to maintain above 80% conversions through 9+ hours of constant power operation. LSCMN 40:40:20 was found to be completely regenerable through calcination at 1000 °C which resulted in the removal of deposited carbon and the re-absorption of the Ni and Co active sites back into the parent perovskite, ready to be reactivated under dry reforming conditions.

Declaration of Competing Interest

A US patent No. US 11,981,565 B2 (issue date May 14, 2024) was awarded based in part on this published research.

Acknowledgements

This work was performed in support of the U.S. Department of Energy's (DOE) Office of Fossil Energy and Carbon Management's (FECM) Carbon Conversion Program and executed through the National Energy Technology Laboratory (NETL) Research and Innovation Center's Carbon Conversion Field Work Proposal.

Crystal structure images generated using CrystalMaker©, Crystal-Maker Software Ltd (www.crystalmaker.com). We also thank Dr. Stephen House and the University of Pittsburgh for TEM analysis and Dr. Bret Howard for XRD expertise.

Supporting Information

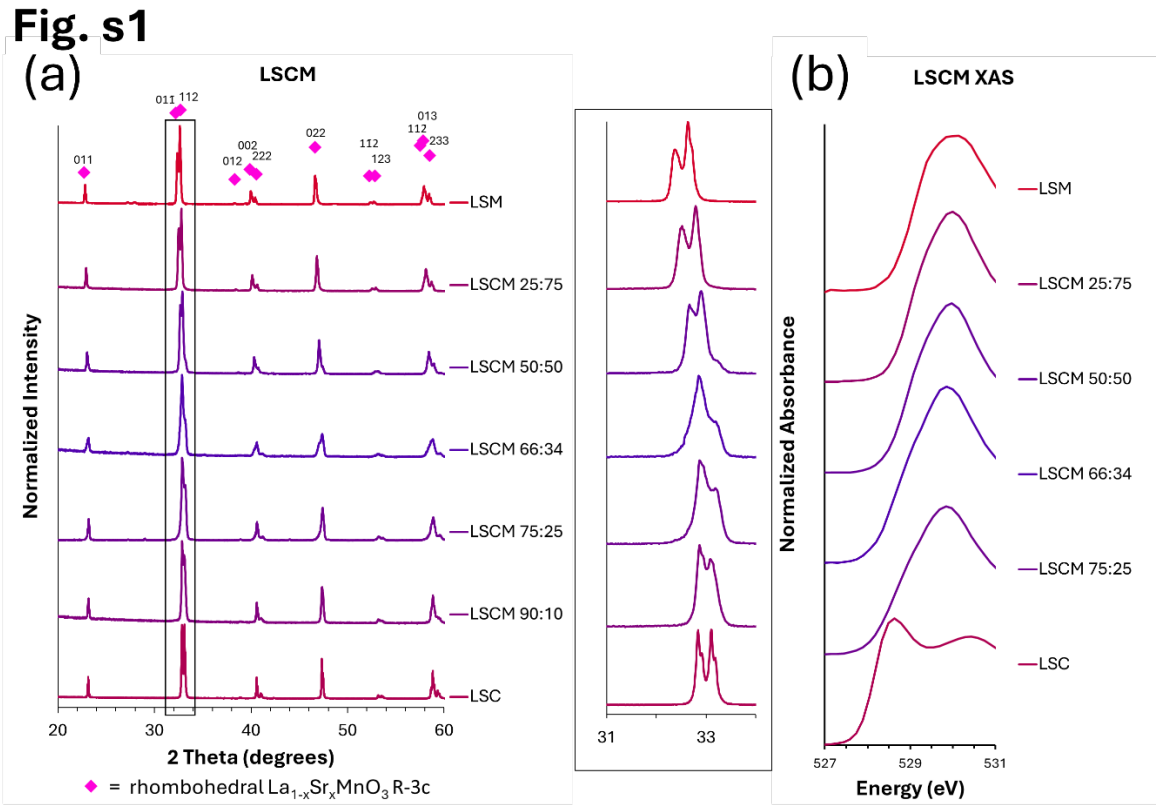

Figure s1. (a) Normalized XRD patterns for all seven compositions of LSM-LSC perovskite series with colors assigned according to MW-DRM performances as shown in Table 4. Magenta diamonds show primary reflections in the rhombohedral structure. Inset shows the primary reflections around 33° of all seven catalysts highlighting both the gradual shift in 2-theta due to ionic radii changes on substitution, and the gradual shift to almost a single reflection peak at LSCM 66:34. (b) Normalized XAS spectra for all seven compositions of LSM-LSC perovskites.

Fig. s2

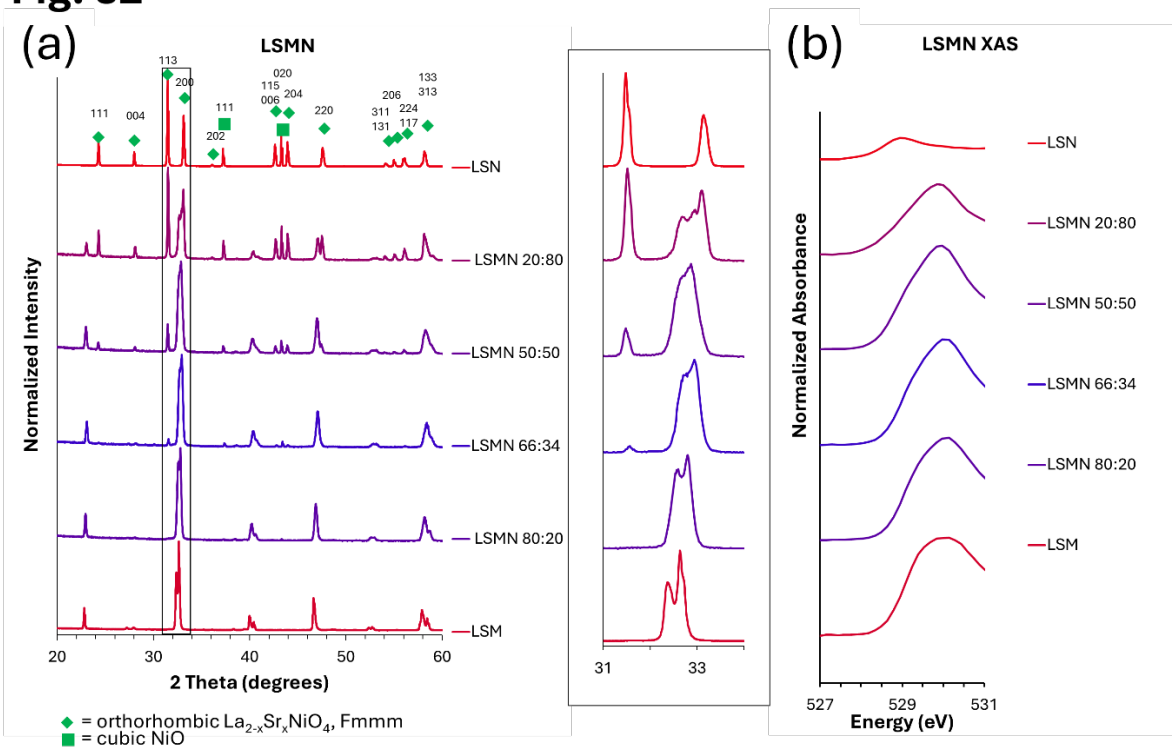

Figure s2. (a) Normalized XRD patterns for all six compositions of LSM-LSN perovskite series with colors assigned according to MW-DRM performances as shown in Table 4. Green squares show primary reflections for cubic NiO while green diamonds show the orthorhombic Ruddlesden-Popper structure reflections. Inset shows the primary reflections around 33° of all six catalysts highlighting both the gradual shift in 2-theta due to ionic radii changes on substitution, and the gradual shift to almost a single reflection peak at LSMN 66:34. (b) Normalized XAS spectra for all six compositions of LSM-LSN catalysts.

Fig. s3

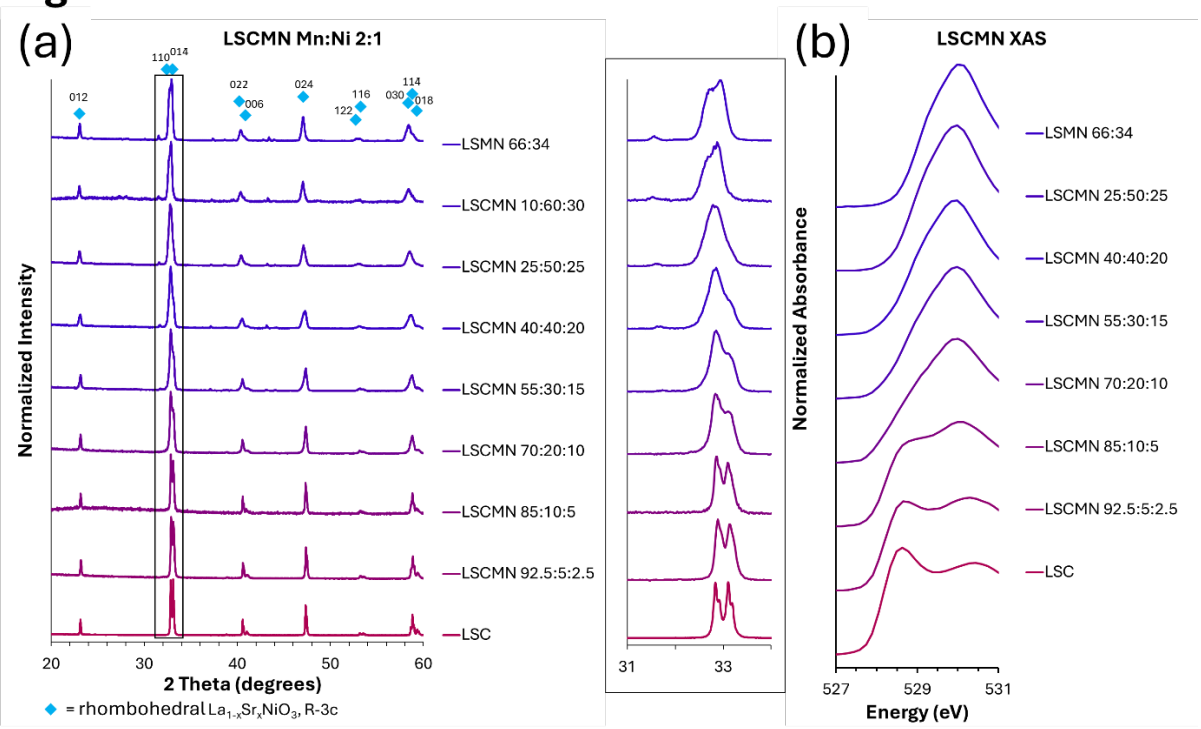

Figure s3. (a) Normalized XRD patterns for all nine compositions of LSM-LSN-LSC perovskite series with the Mn:Ni ratio fixed at 2:1 and with colors assigned according to MW-DRM performances as shown in Table 4. Blue diamonds show the rhombohedral perovskite structure reflections of LSN. Inset shows the primary reflections around 33° of all nine catalysts highlighting both the gradual shift in 2-theta due to ionic radii changes on substitution, and the gradual shift to almost a single reflection peak at LSCMN 40:40:20 to LSMN 66:34. (b) Normalized XAS spectra for all nine compositions of LSM-LSN-LSC perovskites.

Fig. s4

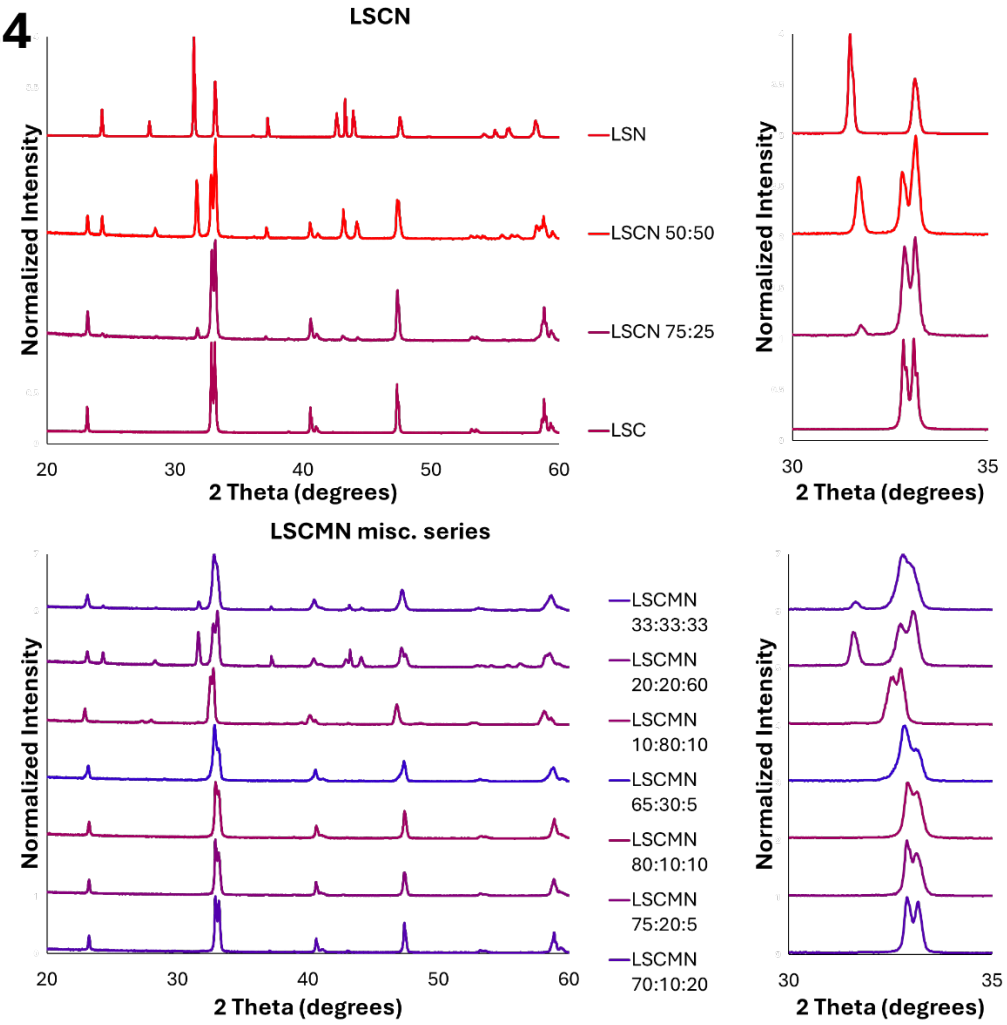

Figure s4. (a) Normalized XRD patterns for remaining 11 compositions and with colors assigned according to MW-DRM performances as shown in Table 4. Top series shows the four compositions in the LSC-LSN series with inset showing the primary reflections near 33°. Bottom series show the seven compositions in the LSM-LSN-LSC series where the Mn:Ni ratio was not at 2:1 with the inset again showing the primary reflections near 33°.

Fig. s5

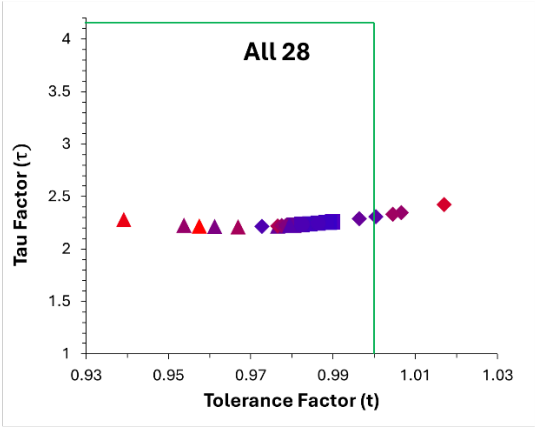

$$\tau = \frac{r_X}{r_B} - n_A\left(n_A - \frac{\frac{r_A}{r_B}}{\ln\left(\frac{r_A}{r_B}\right)}\right)$$

#	Name	Co	Mn	Ni	R_b	R_b/R_O	t	tau
1	LSC	100	0	0	0.61	0.43571	0.97659	2.2194
2	LSCM 90:10	90	10	0	0.602	0.43000	0.98049	2.2274
3	LSCM 75:25	75	25	0	0.59	0.42143	0.98641	2.2443
4	LSCM 66:34	66	34	0	0.5828	0.41629	0.98999	2.2573
5	LSCM 50:50	50	50	0	0.57	0.40714	0.99642	2.2858
6	LSCM 25:75	25	75	0	0.55	0.39286	1.00664	2.3444
7	LSM	0	100	0	0.53	0.37857	1.01707	2.4210
8	LSMN 80:20	0	80	20	0.562	0.40143	1.00048	2.3072
9	LSMN 66:34	0	66	34	0.584	0.41743	0.98919	2.2543
10	LSMN 50:50	0	50	50	0.61	0.43571	0.97659	2.2194
11	LSMN 20:80	0	20	80	0.658	0.47000	0.95381	2.2246
12	LSN	0	0	100	0.69	0.49286	0.93921	2.2785
13	LSCMN 70:10:20	70	10	20	0.618	0.44143	0.97272	2.2139
14	LSCMN 75:20:5	75	20	5	0.598	0.42714	0.98246	2.2324
15	LSCMN 80:10:10	80	10	10	0.61	0.43571	0.97659	2.2194
16	LSCMN 65:30:5	65	30	5	0.59	0.42143	0.98641	2.2443
17	LSCMN 10:80:10	10	80	10	0.61	0.43571	0.97659	2.3313
18	LSCMN 20:20:60	20	20	60	0.642	0.45857	0.96129	2.2127
19	LSCMN 33:33:33	33	33	33	0.6039	0.43136	0.97956	2.2253
20	LSCMN 92.5:5:2.5	92.5	5	2.5	0.608	0.43429	0.97756	2.2211
21	LSCMN 70:20:10	70	20	10	0.602	0.43000	0.98049	2.2274
22	LSCMN 40:40:20	40	40	20	0.594	0.42429	0.98443	2.2380
23	LSCMN 25:50:25	25	50	25	0.59	0.42143	0.98641	2.2443
24	LSCMN 10:60:30	10	60	30	0.586	0.41857	0.98839	2.2513
25	LSCMN 85:10:5	85	10	5	0.606	0.43286	0.97854	2.2231
26	LSCMN 55:30:15	55	30	15	0.598	0.42714	0.98246	2.2324
27	LSCN 75:25	75	0	25	0.63	0.45000	0.96697	2.2105
28	LSCN 50:50	50	0	50	0.65	0.46429	0.95754	2.2174

Figure s5. Plot and table of Tau factors and tolerance factors for all 28 catalysts described in this study. All 28 materials had Tau factors well below the 4.18 limit proposed as a limit for stable perovskite formation.

Fig. s6

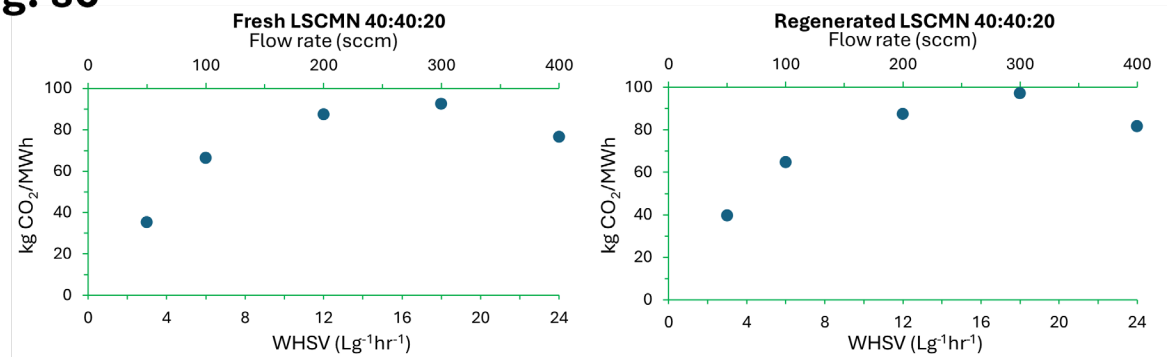

Figure s6. Catalyst performance vs. flow rate/space velocity for fresh $La_{0.8}Sr_{0.2}Co_{0.4}Mn_{0.4}Ni_{0.2}O_3$ and the same catalyst after recalcining at 1000 °C and freshly regrinding. Peak performance was slightly higher after regenerating the sample but was within a standard deviation range for peak performance in both cases.

References

[1] S. Hernández, M.A. Farkhondehfal, F. Sastre, M. Makkee, G. Saracco, N. Russo, Syngas production from electrochemical reduction of CO2: current status and prospective implementation, Green Chemistry, 19 (2017) 2326-2346.
[2] K. Gunawardane, Evolution of hydrogen energy and its potential opportunitites around the globe, in: M.M.K. Khan (Ed.) Hydrogen Energy Conversion and Management, Elsevier2024.
[3] H. Karibe, S. Sair, A. Faik, H.A. Ousaleh, Electrified steam methane reforming: A review of heating technologies, challenges, and prospects, International Journal of Hydrogen Energy, 133 (2025) 200-213.
[4] H. Yang, I.N. Zaini, R. Pan, Y. Jin, Y. Wang, L. Li, J.J.B. Caballero, Z. Shi, Y. Subasi, A. Nurdiawati, S. Wang, Y. Shen, T. Wang, Y. Wang, L. Sandström, P.G. Jönsson, W. Yang, T. Han, Distributed electrified heating for efficient hydrogen production, Nature Communications, 15 (2024).
[5] H. Kozuka, K. Ohbayashi, K. Koumoto, Electronic conduction in La-based perovskite-type oxides, Science and Technology of Advanced Materials, 16 (2015).
[6] J. Ovenstone, J.S. White, S.T. Misture, Phase transitions and phase decomposition of $La_{1-x}Sr_xCoO_{3-\delta}$ in low oxygen partial pressures, Journal of Power Sources, 181 (2008) 56-61.
[7] C.M. Marin, E.J. Popczun, T.-D. Nguyen-Phan, D.N. Tafen, D. Alfonso, I. Waluyo, A. Hunt, D.R. Kauffman, Designing perovskite catalysts for controlled active-site exsolution in the microwave dry reforming of methane, Applied Catalysis B: Environmental, 284 (2021).
[8] V.V.M. Goldschmidt, Die Gesetze der Krystallochemie, Die Naturwissenschaften, 14 (1926) 477-485.
[9] W. Travis, E.N.K. Glover, H. Bronstein, D.O. Scanlon, R.G. Palgrave, On the application of the tolerance factor to inorganic and hybrid halide perovskites: a revised system, Chemical Science, 7 (2016) 4548-4556.
[10] R.D. Shannon, Revised Effective Ionic Radii and Systematic Studies of Interatomic Distances in Halides and Chalcogenides, Acta Crystallographica, A32 (1976) 751-767.
[11] A. Kojima, K. Teshima, Y. Shirai, T. Miyasaka, Organometal Halide Perovskites as Visible-Light Sensitizers for Photovoltaic Cells, Journal of the American Chemical Society, 131 (2009) 6050-6051.
[12] Q. Tai, K.-C. Tang, F. Yan, Recent progress of inorganic perovskite solar cells, Energy & Environmental Science, 12 (2019) 2375-2405.
[13] X. Jiang, S. Qin, L. Meng, G. He, J. Zhang, Y. Wang, Y. Zhu, T. Zou, Y. Gong, Z. Chen, G. Sun, M. Liu, X. Li, F. Lang, Y. Li, Isomeric diammonium passivation for perovskite–organic tandem solar cells, Nature, 635 (2024) 860-866.
[14] L.M. Feng, L.Q. Jiang, M. Zhu, H.B. Liu, X. Zhou, C.H. Li, Formability of ABO3 cubic perovskites, Journal of Physics and Chemistry of Solids, 69 (2008) 967-974.
[15] M.R. Filip, F. Giustino, The geometric blueprint of perovskites, PNAS, 115 (2018) 5397–5402.
[16] A. Kumar, A.S. Verma, S.R. Bhardwaj, Prediction of Formability in Perovskite-Type Oxides, The Open Applied Physics Journal, 1 (2008) 11-19.
[17] C.J. Bartel, C. Sutton, B.R. Goldsmith, R. Ouyang, C.B. Musgrave, L.M. Ghiringhelli, M. Scheffler, New tolerance factor to predict the stability of perovskite oxides and halides, Science Advances, 5 (2019) 1-9.
[18] H. Park, R. Mall, F.H. Alharbi, S. Sanvito, N. Tabet, H. Bensmail, F. El-Mellouhi, Learn-and-Match Molecular Cations for Perovskites, J. Phys Chem A, 33 (2019) 7323-7334.
[19] Q. Tao, P. Xu, M. Li, W. Lu, Machine learning for perovskite materials design and discovery, npj Computational Materials, 7 (2021).
[20] M. Usman, W.M.A.W. Daud, H.F. Abbas, Dry reforming of methane: Influence of process parameters-A review, Renewable and Sustainable Energy Reviews, 45 (2015) 710-744.
[21] S. Shoji, X. Peng, A. Yamaguchi, R. Watanabe, C. Fukuhara, Y. Cho, T. Yamamoto, S. Matsumura, M.-W. Yu, S. Ishii, T. Fujita, H. Abe, M. Miyauchi, Photocatalytic uphill conversion of natural gas beyond the limitation of thermal reaction systems, Nature Catalysis, 3 (2020) 148-153.

[22] S.M. Kim, P.M. Abdala, T. Margossian, D. Hosseini, L. Foppa, A. Armutlulu, W. Beek, A. Comas-Vives, C. Copéret, C. Müller, Cooperativity and Dynamics Increase the Performance of NiFe Dry Reforming Catalysts, Journal of the American Chemical Society, 139 (2017) 1937-1949.
[23] I.V. Yentekakis, G. Goula, M. Hatzisymeon, I. Betsi-Argyropoulou, G. Botzolaki, K. Kousi, D.I. Kondarides, M.J. Taylor, C.M.A. Parlett, A. Osatiashtiani, G. Kyriakou, J.P. Holgado, R.M. Lambert, Effect of support oxygen storage capacity on the catalytic performance of Rh nanoparticles for CO_2 reforming of methane, Applied Catalysis B: Environmental, 243 (2019) 490-501.
[24] K. Li, C. Pei, X. Li, S. Chen, X. Zhang, R. Liu, J. Gong, Dry reforming of methane over $La_2O_2CO_3$-modified Ni/Al_2O_3 catalysts with moderate metal support interaction, Applied Catalysis B: Environmental, 264 (2020) 118448.
[25] S. Chen, J. Zaffran, B. Yang, Dry reforming of methane over the cobalt catalyst: Theoretical insights into the reaction kinetics and mechanism for catalyst deactivation, Applied Catalysis B: Environmental, 270 (2020) 118859.
[26] Z. Bian, Z. Wang, B. Jiang, P. Hongmanorom, W. Zhong, S. Kawi, A review on perovskite catalysts for reforming of methane to hydrogen production, Renewable and Sustainable Energy Reviews, 134 (2020) 110291.
[27] A.N. Petrov, V.A. Cherepanov, A.Y. Zuyev, V.M. Zhukovsky, Thermodynamic Stability of Ternary Oxides in Ln-M-O (Ln = La, Pr, Nd; M = Co, Ni, Cu) Systems, Journal of Solid State Chemistry, 77 (1988) 1-14.
[28] A.N. Petrov, V.A. Cherepanov, A.Y. Zuev, Thermodynamics, defect structure, and charge transfer in doped lanthanum cobaltites: an overview, Journal of Solid State Electrochemistry, 10 (2006) 517-537.
[29] D. Neagu, G. Tsekouras, D.N. Miller, H. Ménard, J.T.S. Irvine, In situ growth of nanoparticles through control of non-stoichiometry, Nature Chemistry, 5 (2013) 916-923.
[30] D. Neagu, T.-S. Oh, D.N. Miller, H. Ménard, S.M. Bukhari, S.R. Gamble, R.J. Gorte, J.M. Vohs, J.T.S. Irvine, Nano-socketed nickel particles with enhanced coking resistance grown *in situ* by redox exsolution, Nature Communications, 6 (2015).
[31] E. Cali, M.P. Thomas, R. Vasudevan, J. Wu, O. Gavalda-Diaz, K. Marquardt, E. Saiz, D. Neagu, R.R. Unocic, S.C. Parker, B.S. Guiton, D.J. Payne, Real-time insight into the multistage mechanism of nanoparticle exsolution from a perovskite host surface, Nature Communications, 14 (2023).
[32] M.K. Nikoo, N.A.S. Amin, Thermodynamic analysis of carbon dioxide reforming of methane in view of solid carbon formation, Fuel Processing Technology, 92 (2011) 678-691.
[33] T.L. LeValley, A.R. Richard, M. Fan, The progress in water gas shift and steam reforming hydrogen production technologies – A review, International Journal of Hydrogen Energy, 39 (2014) 16983-17000.
[34] B.J. Kennedy, P.J. Saines, J. Ting, Q. Zhou, J.A. Kimpton, Structural characterisation of the perovskite series SrxCa1-x-yNdyMnO3: Influence of the Jahn-Teller effect, Journal of Solid State Chemistry, 182 (2009) 2858-2866.
[35] Y. Orikasa, T. Ina, T. Nakao, A. Mineshige, K. Amezawa, M. Oishi, H. Arai, Z. Ogumi, Y. Uchimoto, X-ray Absorption Spectroscopic Study on $La_{0.6}Sr_{0.4}CoO_{3-\delta}$ Cathode Materials Related with Oxygen Vacancy Formation, The Journal of Physical Chemistry C, 115 (2011) 16433-16438.
[36] L. Karvonen, M. Valkeapää, R.-S. Liu, J.-M. Chen, H. Yamauchi, M. Karppinen, O-K and Co-L XANES Study on Oxygen Intercalation in Perovskite $SrCoO_{3-\delta}$, Chemistry of Materials, 22 (2010) 70-76.
[37] J. Suntivich, W.T. Hong, Y.-L. Lee, J.M. Rondinelli, W. Yang, J.B. Goodenough, B. Dabrowski, J.W. Freeland, Y. Shao-Horn, Estimating Hybridization of Transition Metal and Oxygen States in Perovskites from O K-edge X-ray Absorption Spectroscopy, The Journal of Physical Chemistry C, 118 (2014) 1856-1863.